Research Square

Preprints are preliminary reports that have not undergone peer review.
They should not be considered conclusive, used to inform clinical practice,
or referenced by the media as validated information.

Embedded 3D-Printed Magnetic Shape-Memory Robots with Frequency-Separated Control for Wireless Luminal Support

Mojun Chen

mjchen@hkust-gz.edu.cn

Hong Kong University of Science and Technology https://orcid.org/0000-0002-2466-6136

Wenrui Zhang

Shiqi Hu

Pohang University of Science and Technology (POSTECH)

Yijie Bian

Hong Kong University of Science and Technology

Mei Zhou

Hong Kong University of Science and Technology

Kai Zhuang

Hong Kong University of Science and Technology

Zeji Sun

Hong Kong University of Science and Technology

Xiao Xiao

Hong Kong University of Science and Technology

Hao Jiang

Hong Kong University of Science and Technology

Shuaiqi Liu

Hong Kong University of Science and Technology

Xiong Zhou

Hong Kong University of Science and Technology

Jizhuang Wang

Jinan University

Li Liu

Harbin Institute of Technology (Shenzhen)

Han Yu

Tianjin University

Article

Keywords: Magnetic microrobots, embedded printing, shape-memory polymers, dual-frequency magnetic actuation, catheter-free thrombectomy

Posted Date: September 17th, 2026

DOI: https://doi.org/10.21203/rs.3.rs-10896653/v1

License: This work is licensed under a Creative Commons Attribution 4.0 International License. Read Full License

Additional Declarations: There is no conflict of interest

Abstract

Current thrombectomy systems depend on catheter–guidewire platforms with full-segment balloon inflation for luminal support, yet these approaches are procedurally complex and poorly suited to tortuous or distal vascular anatomies. Here we present an embedded-printing strategy for magnetically actuated stent-like robots that enables wireless navigation and on-site mechanical deployment without catheters, guidewires or inflatable balloons. Cylindrical shape-memory lattices were direct-ink-written inside a yield-stress Pluronic F-127 support bath from a composite ink comprising a PLA/PLGA matrix, tributyl citrate plasticizer and Fe_3O_4 nanoparticles that functioned simultaneously as magnetic handles and inductive heaters. The thermoreversible nature of the bath permitted release by cooling rather than mechanical excavation, thereby preserving the thin strut architecture. Support-bath rheology and a four-variable printing map afforded reproducible control over strut and node geometry, while ink composition independently tuned the switching temperature, recovery kinetics and maximum temperature achievable under an alternating magnetic field. A quasi-static magnetic field oriented the robot and drove continuous rotation, a field gradient steered the compact device along prescribed trajectories through a printed vascular-mimetic channel network, and a 50 kHz alternating field triggered radial expansion at the target site. Because navigation and deployment leverage distinct physical mechanisms in the same magnetic particles, the two commands remain non-interfering and the device requires no onboard electronics, tethers or inflatable elements. This work establishes an embedded, single-step micro/nanofabrication platform for fully magnetic, catheter-free thrombectomy robots capable of remote steering and shape-recovery-based luminal support.

Introduction

Miniaturized magnetic robots have matured from simple swimmers into architected, multi-modal machines capable of walking, rolling, swimming and navigating through complex environments under programmed field sequences[1–6]. In endovascular applications, helical and drill-type magnetic actuators have penetrated three-dimensional phantom vascular networks, and magnetically navigated devices have now been demonstrated at human scale in hepatic arteries[7–10]. Remote magnetic navigation, by this point, is largely a solved problem.

Yet navigation is only half of an endovascular intervention. A robot intended to provide mechanical support—whether to scaffold a collapsed lumen, hold open a stenosis, anchor a payload against flow, or restore patency during thrombectomy[11–15]—must satisfy a second set of requirements that conflicts with the first. In transit, the device should present a small cross-section, low hydrodynamic drag and sufficient compliance to negotiate tortuous anatomy. After arrival, it must expand into contact with the vessel wall, exert a defined radial force and remain dimensionally stable once the driving field is removed. Mobility favours a small, compliant, low-profile body; support demands a large, stiff, wall-conforming one.

Current thrombectomy and endoluminal support systems resolve this conflict through tethered delivery platforms. Balloon-expandable scaffolds rely on catheter-mounted balloons that plastically enlarge the device at the lesion[16], while self-expanding scaffolds store elastic energy in a constrained delivery sheath and release it on withdrawal[17]. Both approaches are clinically effective, but both are fundamentally tethered: the expansion energy and its trigger travel down a delivery system that must physically reach the target. This requirement becomes the limiting factor in tortuous, small or repeatedly branched anatomies. A growing body of work has therefore sought to move the expansion function out of the delivery system and into the device material itself. Magnetically guided shape-memory micro-anchors have been deployed into micro-vasculature, modular magnetic microrobot systems have transported conventional stents through complex ductal anatomy, and printed polymer scaffolds have been shown to deploy remotely while carrying functional surface chemistry. These advances establish that responsive materials can replace part of the delivery infrastructure. What remains unresolved is the control architecture behind them—specifically, how transport and deployment can be driven through the same magnetic hardware without the two commands interfering, and how the open, thin-strut architecture required for such devices can be manufactured reproducibly from a material that is simultaneously magnetic and thermally switchable.

Thermally activated shape-memory polymers offer a natural basis for the on-command state switch that this application demands. A permanent geometry is fixed during fabrication by a network of physical or chemical netpoints. Heating above a switching transition—typically the glass transition *T*g in amorphous systems—restores segmental mobility so that an external load can impose a temporary geometry; cooling under load re-immobilizes the deformed chains and stores entropic strain energy; reheating releases this energy and drives recovery toward the permanent shape[18,19]. The two states are usefully decoupled: programming sets the temporary state, while printing sets the permanent one.

PLA-based systems are particularly suited to this role because the switching transition can be positioned across a wide, technologically relevant range[18,20]. Citrate plasticizers such as tributyl citrate increase free volume and depress *T*g almost monotonically with loading, while copolymerized glycolide units disrupt chain regularity, suppress crystallization and alter both recovery rate and recoverable strain[21]. Dispersing Fe_3O_4 nanoparticles into such a matrix adds two physically distinct functions. Under a quasi-static magnetic field, the particle ensemble experiences a torque proportional to field magnitude and a translational force proportional to field gradient; under a high-frequency alternating magnetic field, the same particles dissipate energy through hysteresis and relaxation losses, heating the surrounding polymer volumetrically rather than from an external surface[22,23]. One composite therefore supports two control channels separated by frequency rather than by hardware—the low-frequency channel moving the robot and the high-frequency channel triggering it. This frequency separation is the central organizing principle of the present work.

Realizing this architecture requires an open cylindrical lattice with struts on the order of one hundred micrometres, printed from an ink that is both heavily loaded with dense inorganic particles and dissolved

in a volatile solvent. Almost every span in such a lattice is unsupported and obliquely oriented, so each freshly written strand must hold its position throughout consolidation. Printed in air, this is impossible: strands sag under gravity before solidification, capillary forces contract unsupported spans, the moving nozzle drags previously deposited material out of registration, and rapid solvent flash produces skinning and nozzle blockage. These failures share a single cause—the strand is left to support itself between deposition and solidification—and are therefore not solved simply by faster-setting or stiffer formulations. What is needed instead is an external medium that carries the strand until it can carry itself, applies that support in every direction rather than only from below, and then leaves without becoming part of the structure. A yield-stress fluid satisfies all three requirements. It behaves as an elastic solid below its yield stress, fluidizes locally where the moving nozzle and emerging strand exceed that stress, and re-solidifies immediately behind them, so the growing lattice is held continuously throughout the build and released only when the bath itself is removed. Embedded printing in such media has been used to write hydrogels[24], elastomers[25–27], cell-laden constructs[28] and thermoplastics[29] in freeform geometries that would otherwise be unprintable. When the ink is PLA dissolved in dichloromethane[29,30] and the bath is aqueous, a further mechanism operates: DCM is miscible with the nonsolvent, so immersion precipitation contributes to filament consolidation alongside mechanical support. Filament formation under these conditions depends jointly on bath rheology, ink rheology, nozzle wetting, extrusion pressure and path speed, with characteristic defect modes appearing outside a bounded process window; these variables must therefore be mapped as a coupled system rather than optimized individually.

In this work, we develop an embedded-printing strategy for magnetically actuated, stent-like lattice robots that enables wireless navigation and on-site mechanical deployment without catheters, guidewires or inflatable balloons. Cylindrical shape-memory lattices are direct-ink-written inside a thermoreversible Pluronic F-127 support bath from a composite ink comprising a PLA/PLGA matrix[31], tributyl citrate plasticizer and Fe_3O_4 nanoparticles that function simultaneously as magnetic handles and inductive heaters. The yield-stress nature of the bath permits release by cooling through its gel–sol transition rather than by mechanical excavation, thereby preserving the thin strut architecture. Support-bath rheology and a four-variable printing map spanning nozzle diameter, extrusion pressure, path speed and interfilament gap afford reproducible control over strut and node geometry, while ink composition independently tunes the switching temperature, recovery kinetics and maximum temperature achievable under an alternating magnetic field. With the material so programmed, a quasi-static magnetic field orients the compact robot and drives continuous rotation, a field gradient steers it along prescribed trajectories and through a printed vascular-mimetic channel network, and a 50 kHz alternating field triggers radial expansion at the selected site while preserving axial length. Because navigation and deployment leverage distinct physical mechanisms in the same magnetic particles, the two commands remain non-interfering, and the device requires no onboard electronics, tethers or inflatable elements. This work establishes an embedded, single-step micro/nanofabrication platform for fully magnetic, catheter-free robots capable of remote steering and shape-recovery-based luminal support. We expect this magnetothermal lattice robot to broaden the design space of untethered endovascular devices, with

its freeform manufacturing of open lattice architectures, compositional programmability of switching behaviour and frequency-separated magnetic control advancing the practical realization of remotely deployable platforms for thrombectomy and mechanical support in confined, hard-to-reach anatomies.

Embedded printing yields free-standing magnetothermal lattice robots

The fabrication route was designed around a geometry that is essentially unprintable in air. A cylindrical lattice consists almost entirely of unsupported, obliquely oriented spans, each of which must hold position while a solvent-rich, particle-loaded strand consolidates. We therefore submerged the nozzle in a Pluronic F-127 bath and traced the helical and circumferential toolpaths within it (Fig. 1a). Where the nozzle moves and extrudes, the applied stress exceeds the bath yield stress, the medium fluidizes, and both nozzle and emerging strand advance. Behind the nozzle, the stress falls, the network re-forms, and the deposited strand is held in place. The support is omnidirectional—a necessity because the critical spans in a lattice are neither vertical nor horizontal. It is also temporary, being removed later by a purely thermal step. Two failure modes common to air printing—progressive sagging of the newest layer and compressive collapse of the lower courses under the weight of the unfinished structure—are thereby eliminated simultaneously.

Each ink constituent serves a separable function (Fig. 1b). PLA forms the primary thermoplastic framework and defines the permanent printed geometry through its entangled, partially crystalline network. PLGA is blended with PLA to modulate chain mobility, suppress crystallinity, and adjust recovery kinetics without altering the solvent-processing route or introducing additional chemical species. tBC acts as an internal plasticizer, increasing free volume and depressing the switching transition into a range accessible to modest remote heating. Fe_3O_4 nanoparticles provide magnetic susceptibility for torque- and gradient-based manipulation, while also supplying hysteretic loss for AMF-driven volumetric heating. Pluronic F-127, shown separately in Fig. 1b, is not part of the device at all; it is a sacrificial process material whose inverse thermoreversible gelation is exploited twice—first to support the print at room temperature and then to release it upon cooling[32,33].

The composite was formulated in dichloromethane so that PLA, PLGA, and tBC form a single continuous phase around the dispersed magnetic particles. Because deposition occurs into an aqueous medium, both solvent loss and nonsolvent exchange contribute to strand consolidation while the bath maintains external mechanical support. This dual consolidation mechanism is consistent with earlier immersion-precipitation printing of PLA/DCM inks. The detailed printing process is shown in Fig. 1c (Supplementary Video 1). Quantifying the relative contributions of evaporation versus precipitation in the present system would require direct residual-solvent quantification and cross-sectional porosity analysis, which we identify as a direction for future work.

After printing, the lattice remained fully embedded in the optically transparent support matrix, visible as a dark cylinder suspended within the bath (Fig. 1d). Harvesting exploited the inverse thermoreversibility of

Pluronic F-127. Cooling the container to 0–4°C converts the micellar cubic gel into a low-viscosity sol, releasing the structure without mechanical intervention (Fig. 1e). Repeated rinsing in deionized water removed visible residue, and the harvested cylinders stood freely with open, unoccluded pores.

Sacrificial materials that must be aggressively dissolved or mechanically excavated impose damaging loads on the very thin, high-aspect-ratio struts that subsequently store and release the shape-memory strain. A purely thermal release avoids this damage mode; the single modification that transformed the intact recovery of open lattices from an occasional outcome into a routine one.

Figure 1f summarizes the intended operating cycle in a planar channel network with straight, curved, and bifurcating segments. The lattice is programmed into a compact, radially collapsed transport state and introduced with its long axis parallel to the local channel centreline. A magnetic field gradient translates it along the channel toward a target. Local AMF exposure then heats the composite above its switching transition, restoring the printed diameter so that the lattice expands laterally into contact with both sidewalls and acts as a local support. The horizontal orientation is functionally essential: because recovery is radial, only a laterally lying cylinder converts recovered diameter into wall contact across the channel cross-section, analogous to an expanding balloon or stent; an upright cylinder would merely elongate vertically. Figure 1f is a design schematic, with the corresponding navigation and deployment experiments presented in Fig. 4.

Support-bath rheology sets the fabrication window

A support bath has to satisfy two requirements that pull against each other. It must yield readily around the moving nozzle, since excessive drag deflects the nozzle, distorts the toolpath and can tear previously written features. The nozzle itself was rendered hydrophobic by vapour-phase silanization before use, which suppressed wetting of the outer wall by the DCM-based ink and gave continuous filaments in place of the intermittent, bead-forming deposition seen with untreated nozzles (Figure S2 and S3). Its post-yield structure must also rebuild fast enough to immobilize a strand before that strand can sag, drift or coalesce with its neighbours. Pluronic concentration is the available design variable, and we mapped its effect across 18, 20, 22, 25 and 30 wt%.

Oscillatory stress sweeps showed a progressive strengthening of the solid-like state with concentration (Fig. 2a). In the low-stress plateau, the storage modulus G' rose by close to two orders of magnitude across the series, from about 5.5×10^2 Pa at 18 wt% to 3.77×10^4 Pa at 30 wt%. The $G' = G''$ crossover, taken here as the operational yield stress σ_y, rose correspondingly from about 12.9 to 930 Pa. Every formulation was solid-like at rest and fluid-like above its crossover[34], so concentration tunes the magnitude of the yield stress and not the qualitative response. At 18 wt% the bath offered almost no resistance to nozzle motion but also little restoring stress, so it could not arrest a dense, DCM-swollen strand against gravity. Strands sank and the lattice lost registration. At 30 wt% the bath supported the structure emphatically, but the nozzle had to overcome a yield stress approaching 1 kPa, which produced visible toolpath deflection and crevasse formation along the nozzle track. The 22 wt% formulation sat

between the two, with σ_y near 275 Pa and a rest modulus of about 1.5×10^4 Pa, and was used for all subsequent lattice printing.

The rate at which the fluidized bath re-solidifies was measured from the transient response to a step decrease in shear rate from 10 to 0.01 s^{-1} (Fig. 2b). Apparent viscosity stayed near 39 Pa s during the high-rate interval, then rose steeply once the rate dropped, exceeding 10^4 Pa s within 0.07 s and remaining in that range for the rest of the recorded interval. The earliest sub-decisecond points are convolved with instrument inertia and should not be read as an intrinsic relaxation time, but the measurement does place an upper bound on the rebuild time of order 10^{-1} s.

At the selected translation speed of 1.0 mm s^{-1} with a 150 μm nozzle, the nozzle clears its own diameter in roughly 0.15 s. Rebuild is faster than nozzle clearance, and that is the condition required for the crevasse opened by the nozzle to close upon the strand instead of behind it.

A printing operation fluidizes and re-solidifies the same bath volume many times, since every crossing of a previously written region does so again. Alternating low-strain (0.01%) and high-strain (100%) intervals over five complete cycles produced a fully reversible modulus response (Fig. 2c). During low-strain intervals G' recovered to about 1.3×10^4 Pa with $G' > G''$ throughout. During high-strain intervals G' dropped by more than two orders of magnitude and fell below G'', indicating complete fluidization, and the applied shear stress tracked the same square-wave pattern on the right axis. No systematic degradation of the recovered plateau appeared across cycles. The bath fluidizes and rebuilds by reversible disruption of the micellar network, not by irreversible fracture, and it can be traversed repeatedly during a multi-layer build without cumulative loss of support.

A four-variable process map converts printing parameters into geometry

With the bath fixed at 22 wt%, we mapped the extrusion variables that determine whether a filament forms and, once it forms, what its dimensions are. Printability depended jointly on nozzle diameter and pneumatic pressure (Fig. 2d). The transition from failure to continuous extrusion fell from about 4.0 psi for the 110 μm nozzle to 1.5 psi for the 250 μm nozzle. Below the boundary, extrusion was absent or intermittent and produced beaded or discontinuous tracks. Above it, continuous filaments were obtained across the full pressure range tested. The trend follows from the strong dependence of pressure-driven flow on channel radius. A larger bore reduces the pressure needed to sustain a given throughput, so the threshold falls as the nozzle opens. We treat the dashed boundary in Fig. 2d as a guide to the observed classification transition and not as a constitutive prediction. The classification is binary and human-assigned, and additional repeats near the boundary would be needed to locate it.

Within the printable region, strut width was continuously tunable through pressure and translation speed (Fig. 2e). Increasing pressure increased width at every speed, while increasing speed reduced the material deposited per unit path length and narrowed the strut. Across the map a single nozzle spanned

strut widths from 21.4 to 275.7 μm, roughly one-seventh to nearly twice the nozzle diameter. The two limiting behaviors have different origins. Widths well below the nozzle diameter, obtained at high speed and low pressure, reflect drawdown. The strand is stretched axially by the moving nozzle faster than it is replenished, and it thins before the surrounding bath and the incipient precipitation front arrest its cross-section. Widths above the nozzle diameter, obtained at low speed and high pressure, reflect over-deposition, in which material is supplied faster than the path advances and the strand spreads laterally within the yielded envelope. Neither regime is inherently defective, but they respond differently to perturbation. Drawn strands neck and break. Over-deposited strands thicken the nodes and occlude the pores[35]. A robust operating point should be set between them.

The condition selected for lattice fabrication, 10 psi and 1.0 mm s^{-1}, produced 157.8 ± 3.7 μm struts (mean ± s.d., n = 5), close to the 150 μm nozzle bore. CAD strut dimensions can therefore be specified directly in terms of nozzle diameter without an empirical correction factor, and the process sits at the balance point between the two failure-prone extremes.

Mechanical integrity in a lattice is carried by the fused nodes where obliquely oriented struts cross, and node quality is set by the programmed gap between neighboring paths. Measured connection width stayed near 268 μm at gaps of 0.2 and 0.3 mm, then fell steadily to 59.8 μm at 0.6 mm (mean ± s.d., n = 5; Fig. 2f). The plateau at small gaps indicates that paths closer than roughly one strut width merge into a single wider feature, so the programmed gap is no longer resolved. Beyond about 0.3 mm the paths stay distinguishable and contact only over a shrinking overlap region. The scatter followed the same trend, spanning roughly 185–350 μm at 0.2 mm but only 55–70 μm at 0.6 mm, so the merged regime is both wider and substantially less reproducible.

Small gaps give robust, defect-tolerant fusion but thicken the nodes, reduce porosity and stiffen the lattice, which raises the force needed to program the compact state and can suppress recovery. Large gaps preserve open cells and compliance but approach a disconnection threshold at which the structure loses load-path continuity. Because node width and strut width derive from the same deposition physics, the lattice design cannot be specified from nominal CAD dimensions alone. It has to be specified from the measured joint relationship among pressure, speed, filament width and fusion distance. Four machine settings are thereby converted into two geometric outputs, which in turn determine the mechanical and shape-memory behavior analyzed below.

tBC sets the switching temperature; PLGA sets the recovery kinetics

The robot must stay dimensionally stable throughout navigation, which may take tens of seconds in a fluid whose temperature is not controlled, yet soften promptly once AMF heating begins. These are conflicting demands on one transition temperature, and meeting both requires that the transition be placed deliberately instead of inherited from the base polymer. Neat PLA has a glass transition near 60°C[21], far above any temperature that remote heating can safely reach in a fluid environment. Plasticization is a prerequisite here, not a refinement.

Tributyl citrate provided that control. In offset DSC traces, the weak low-temperature transition shifted from about 40°C at 15 wt% tBC to 28°C at 30 wt% (Fig. 3a), an almost linear depression of roughly 0.8°C per weight percent. The mechanism is the conventional free-volume one. The small, flexible citrate ester inserts between polymer chains, increases interchain separation and lowers the temperature at which cooperative segmental motion becomes possible. We report these values as approximate switching indicators and not as precise thermodynamic transitions, since they were read from modest baseline perturbations superimposed on the heat-flow trace and not from sharp calorimetric features. The strong endotherm near 155–160°C corresponds to melting of the crystalline PLA fraction and is not the transition used for programming.

The 20 wt% tBC composition was selected because it places the switching transition near 37°C, which resolves the stability and responsiveness conflict from both sides. Since 37°C is comfortably above laboratory ambient, the programmed compact state stays fixed indefinitely during handling and navigation without refrigeration or restraint. Since it is only a few degrees above ambient, recovery is triggered by heating to just past 40°C, a target the magnetothermal system reaches readily and one that keeps peak temperature modest. Higher tBC would make the device easier to trigger but marginally stable at room temperature. Lower tBC would demand a thermal excursion that the particle loading cannot deliver.

Both the completeness and rate of stored-strain release are governed by the PLGA fraction, with this dependence exhibiting strongly non-monotonic behavior (Fig. 3b). All five compositions recovered from the programmed state on heating, but they separated in both rate and plateau. The 40 wt% formulation showed the fastest early response but levelled off near 83%. The 30 wt% formulation was initially slower yet continued to recover well past the point at which the others had saturated, reaching about 95% by 40 s, the highest final value in the series. The remaining compositions plateaued between 66 and 75%. The 50 wt% formulation was among the fastest at 5 s yet ended with the lowest final recovery, so early rate and ultimate recoverability are separately controlled quantities that can be traded against each other.

The non-monotonic behavior indicates that PLGA does more than soften the matrix. Glycolide units disrupt the stereoregularity of the PLA chain, suppressing crystallization and raising amorphous chain mobility. At low PLGA content the matrix retains substantial crystallinity, mobility is insufficient for complete strain release within the observation window, and recovery stalls short of the permanent shape. At intermediate content, mobility is high enough for near-complete release while enough physical netpoints, meaning residual crystallites and entanglements, survive to store and transmit the entropic restoring force. At high content, crystallinity is suppressed further and the netpoint density that anchors the permanent shape itself eroded, so part of the imposed deformation is dissipated as permanent viscoplastic flow and never recovered. The optimum reflects a competition between mobility, which PLGA increases, and netpoint density, which PLGA decreases. The 30 wt% composition sits at that optimum and was adopted for all device fabrication.

Time-resolved imaging of the same composition series gives a direct visual counterpart to the angle-based curves (Fig. 3e). Each row tracks one PLGA fraction from 0 to 30 s during AMF exposure, with the instantaneous strut angle marked. The 30 wt% row shows the most complete angular closure over the interval, while both lower and higher fractions retain visibly larger residual angles at 30 s, in agreement with the plateau values in Fig. 3b.

Recovery must also be symmetric and must preserve node connectivity, which the recovery ratio alone cannot capture. A lattice that recovers 90% of its angle while buckling locally, or with one side recovering ahead of the other, will not make uniform wall contact no matter how favorable its scalar recovery ratio looks. We therefore treat angle-recovery as a screening rather than a deployment metric, and identify recovered diameter, axial shortening, cell distortion, and radial force as the quantities that need to be included for device-level qualification.

Fe_3O_4 loading couples the magnetic input to the thermal transition

Particle loading needs to be high enough for AMF exposure to push the composite beyond the pre-established switching transition, while remaining low enough to avoid compromising printability and mechanical integrity. Increasing the nominal Fe_3O_4:PLA mass ratio from 0.25 to 1.00 raised the steady-state magnetothermal temperature from 31.3 to 41.5°C (Fig. 3c). Recovery ratio increased in parallel, from 15.7 ± 7.4% to 75.5 ± 7.5% (mean ± s.d., n = 5). Infrared thermography confirmed that heating was localized to the specimen and did not reflect bulk warming of the surroundings, which is the expected signature of volumetric induction heating in a discrete magnetic body.

A temperature rise of only 10.2°C across the series produced a nearly fivefold increase in recovery, and the steepest gain occurred as the temperature crossed the 37°C transition identified by DSC. The behavior is threshold-like, not proportional. Below the transition, segmental mobility is negligible, and stored strain cannot be released regardless of exposure duration. Accordingly, the modest recovery observed at low particle loading reflects only surface-proximal material and local heterogeneity. Above the transition, the whole cross-section becomes mobile and recovery proceeds to the limit set by netpoint density. Fe_3O_4 loading is thus a requirement to clear a compositionally determined threshold, not a continuous performance dial, and because tBC sets where that threshold lies, the two variables have to be specified jointly. A device with insufficient particle loading fails categorically, not gradually.

At high solids fraction, however, the ink becomes prone to particle aggregation and nozzle clogging, and the printability boundary of Fig. 2d shifts upward in pressure. The composite also stiffens as the non-deformable phase fraction grows, which raises the force needed to program the temporary state and reduces the polymer volume available to store recoverable strain. The 1.00 ratio used here sits at the upper end of the reliably printable range for this formulation. Extending the accessible temperature range further would be better pursued through improved particle dispersion or heating efficiency, such as a narrower size distribution, higher-loss compositions or surface functionalization against agglomeration, than by adding mass.

The complete thermomechanical cycle

Figure 3d summarises the four-step operational cycle of the device. In State 1, the as-printed expanded lattice corresponds to the permanent shape. Held below Tg in the glassy regime, the network consists of low-mobility polymer chains physically cross-linked by crystallites and entanglements, with tBC and Fe_3O_4 particles homogeneously dispersed throughout. Upon heating above Tg (State 2), the matrix transitions to a rubbery, high-mobility state. Under moderate radial compressive loading, the lattice diameter decreases; chains undergo deformation yet netpoints are preserved, so strain is stored entropically with no dissipative loss. In State 3, cooling below Tg while maintaining load re-immobilises polymer chains and fixes the compact temporary shape. Even after load removal, the printed diameter is not recovered: the intrinsic restoring force cannot overcome the mechanical resistance of the vitrified matrix. The resulting transport configuration is stable indefinitely at ambient temperature. For State 4, AMF excitation generates heat within Fe_3O_4 particles through hysteresis and relaxation losses. This internal heating raises the matrix above Tg, reinstates chain mobility, and enables the stored entropic driving force to revert the structure toward its original printed geometry.

Permanent shape is established during printing by network architecture and netpoint distribution, whereas temporary shape is encoded during mechanical programming by applied loading. Accordingly, one printed construct can achieve multiple transport configurations without repeated fabrication. Heat is generated volumetrically from embedded particles rather than external surfaces. For a 160 μm-thick strut, thermal gradients are therefore negligible, and shape-recovery kinetics are limited by chain dynamics instead of thermal conduction. This accounts for the ten-second recovery timescale observed under modest temperature changes, and constitutes the primary benefit of magnetothermal triggering compared with external thermal stimulation in fluid media, where the surrounding environment acts as an effective heat sink.

Quasi-static field direction controls heading; a rotating field drives continuous rotation

The same Fe_3O_4 phase responds to low-frequency and high-frequency magnetic inputs through different physical mechanisms, so the two can be issued independently without cross-talk. Under a quasi-static field, an anisotropic magnetic body experiences a torque $\boldsymbol{\tau} = \mathbf{m} \times \mathbf{B}$ that rotates its net moment toward the field direction, and a force $\mathbf{F} = \nabla(\mathbf{m} \cdot \mathbf{B})$ that drives it along the field gradient. Torque sets orientation and gradient sets position. Because the lattice is a slender cylinder with strong shape anisotropy, its long axis provides a well-defined and optically legible pose indicator (Fig. 4a).

Changing the direction of the applied field reoriented the compact lattice reliably, and the robot long axis tracked the commanded direction (Fig. 4e, first three panels; Supplementary Video 2). Successive frames illustrate the robot oriented at different headings (oblique, diagonal, and normal with respect to the substrate axis), as indicated by red arrows. Reorientation behavior was reproducible: resetting the magnetic field to an earlier direction reverted the robot to the corresponding heading. Neither bistability

nor heading ambiguity was detected. This observation supports the scenario where the body's shape anisotropy dominates over any residual anisotropy originating from particle arrangement.

A continuously rotating field instead produced continuous axial rotation of the body (Fig. 4e, final two panels, circular red arrows; Supplementary Video 3). Under low-speed rotating fields, the robot synchronously tracks field rotation, its long axis retaining a fixed phase offset with respect to the field orientation. This actuation mode differs fundamentally from reorientation and is not simply its fast-operating counterpart. Reorientation converges to static equilibrium; by contrast, rotation corresponds to a driven steady state governed by balance between magnetic torque and viscous drag. Rotation also delivers practical mechanical benefits: long-axis rotation enables dislodgement of the robot when snagged on wall protrusions, and surface-rolling contact supports a gradient-free locomotion mechanism.

Collectively, these two behaviors furnish the rotational degrees of freedom essential for controlled transport operations. Full characterization of this rotational channel — covering angular deviation from commanded direction, settling time, and step-out frequency (the limit beyond which magnetic torque fails to overcome viscous drag) — necessitates calibrated magnetic-field mapping and high-frame-rate orientation tracking.

Gradient-driven navigation along prescribed trajectories and through channel networks

Translation requires a field gradient, which must steer the robot through the corners, reversals and repeated heading changes that a real path imposes (Fig. 4b). We tested this against a deliberately unforgiving target, writing the nine-character string "HKUST(GZ)" by steering the compact robot along the outline of each character in sequence (Fig. 4f; Supplementary Video 4). The robot began at the right of the field of view, was steered leftward along the full string, then traced each character in turn, covering the vertical strokes and crossbar of H, the diagonal limbs of K, the U-turn of U, the double reversal of S, the perpendicular strokes of T, the closed curve of G, the diagonal of Z and the enclosing parentheses. Each panel shows the robot, circled, at a successive stage with its executed path overlaid as a dashed red line.

The trajectory contained straight segments in four orientations, acute and obtuse corners, complete direction reversals and closed curves. The robot executed all of them without becoming trapped, stalling or needing manual repositioning, and the character forms are legible in the executed paths, so arbitrary planar trajectories could be followed and not merely net displacement produced.

We then imposed lateral confinement (Fig. 4c, g). A FDM-printed vascular-mimetic channel network containing straight segments, curves and a bifurcation was filled with fluid, and the compact robot was navigated through it under top-view observation. Sequential frames at 1 s intervals (Fig. 4g, 0–5s; Supplementary Video 5) show the robot traversing the network from an interior position to the far end of

the phantom, passing through curved segments and negotiating the bifurcation region. Traversal of the imaged path took 5 s, and the robot held its long axis approximately parallel to the local channel centerline throughout, which is the orientation required for radial deployment to translate into bilateral wall contact.

In open space a heading error produces a proportional path error, whereas in a channel the walls both constrain and disturb. Small errors are corrected passively, but contact friction is introduced, and at the bifurcation there is a genuine branch-selection decision that the gradient direction must resolve.

The open-top geometry permits unobstructed top-view imaging and direct optical measurement of robot width during deployment, which a sealed channel of this scale would not, at the cost of removing the upper wall. The platform is a channel-confinement mechanics testbed and not a vascular model, and the final section addresses that limitation directly.

AMF exposure triggers radial deployment at the selected site

Following positional placement, the robot executes geometric reconfiguration in response to magnetic commands (Fig. 4d). Frequency separation enables this dual-mode operation without auxiliary hardware. Navigation utilizes quasi-static magnetic fields: direction and gradient produce torque and force with minimal heat generation. For deployment, a 50 kHz alternating magnetic field is applied; its amplitude generates negligible net force but induces hysteretic energy dissipation within the embedded particle ensemble. Since both commands act on the same material through separate physical pathways, no onboard switching, addressing, or logic hardware is necessary for mode selection.

Deployment characterization was carried out in a 4 mm-wide straight groove. This setup allows unconstrained positioning of the compact robot, while the post-recovery lattice approaches both groove sidewalls. AMF stimulation of a robot held within this groove initiates radial lattice expansion (Fig. 4h; Supplementary Video 6). Time-lapse frames acquired at 0, 3, 9, and 18 s capture gradual lateral growth; red double-headed arrows mark instantaneous width, measured between outer lattice edges normal to the groove axis. After 18 s of excitation, the programmed transport width of 2.6 mm expands to 3.85 mm, yielding an expansion ratio of 0.48; the final width fills 96.1% of the groove. Detectable expansion occurs as early as 3 s (3.33 mm), proceeds to 3.55 mm at 9 s, and then saturates toward its maximum value, so the lattice occupies a markedly larger fraction of the groove compared with the initial state. These dynamics are consistent with the compositional-dependent recovery kinetics in Fig. 3b, where the 30 wt% PLGA formulation completes most shape recovery within 15–20 s. Accordingly, shape-recovery performance obtained from free-standing samples is maintained under fluid-phase confinement and near-wall boundary conditions.

The as-printed permanent geometry is a larger-diameter cylinder with unchanged length. Mechanical programming compresses the lattice radially without axial stretching; upon recovery, diameter is restored while axial dimension remains nearly invariant. Functionally resembling a self-expanding

scaffold (or balloon), the device modulates channel cross-section without axial elongation — a deformation that would contribute no supportive effect. This characteristic originates from the pre-defined print-time geometry and dictates that the transport-state robot long axis must align parallel to the channel centerline. Uniaxial compression measurements on lattices with varied strut topologies verify that recovered structures support mechanical loads, instead of only recovering their original printed dimensions. Corresponding load-displacement curves and cyclic-response evolution are presented in Figure S5.

Figure 4e-h illustrates the full operational workflow for one device instance: heading control, continuous rotation, predefined-path navigation in open domains, constrained navigation inside branched channel networks, and site-targeted radial deployment. Every function is driven by externally applied magnetic fields. The printed-polymer robot carries no electronics, tethers, embedded balloons, or local power supply. Magnetic inputs are described by their functional mode rather than calibrated absolute values. Full workspace characterization (local field strength, gradient at robot position, and sample-plane AMF amplitude) via field mapping is a prerequisite for cross-system performance comparison. While deployment experiments verify on-site triggered expansion, they do not quantify radial output force or its decay during cooling-induced matrix re-vitrification. Two control experiments are required to eliminate passive relaxation and intrinsic magnetoelastic deformation as confounding contributions: AMF irradiation of an unprogrammed lattice, and navigation-field-only stimulation of a programmed lattice

Conclusion

We developed a single-step embedded-printing platform for magnetothermal shape-memory lattice robots that enables wireless, tether-free and catheter-free mechanical support in confined luminal environments. By decoupling navigation and deployment through frequency-separated magnetic inputs, a quasi-static field orients, rotates and gradient-steers the compact temporary shape through tortuous trajectories, while a 50 kHz alternating field triggers on-site radial expansion of the permanent shape without cross-interference. The thermoreversible Pluronic F-127 support bath preserves the open-lattice architecture during manufacturing, a four-variable printing map affords reproducible control of strut and node geometry, and ink composition provides three independent programming axes—plasticizer content sets the switching temperature, PLGA fraction governs recovery kinetics and Fe_3O_4 loading determines inductive heating efficiency. The resulting device was demonstrated to follow prescribed planar paths, navigate a branched vascular-mimetic channel network and expand radially at the target site while preserving axial length. These results define a manufacturing and actuation framework for remotely deployable, balloon-free endoluminal support. Advancing this concept toward clinical translation will require calibrated workspace field mapping, quantitative radial-force measurement, closed-channel flow testing and systematic biological safety evaluation.

Experimental Section

Materials

Polylactic acid (PLA, Mw ≈ 150000) was purchased from Shanghai Macklin Biochemical Co., Ltd. Poly(L-lactide-co-glycolide) (L-PLGA, inherent viscosity ≈ 0.92 dL/g) was obtained from Jinan Daigang Biomaterial Co., Ltd. Magnetite nanoparticles (Fe_3O_4, particle size 50–300 nm), tributyl citrate (tBC, plasticizer), and dichloromethane (DCM, UltraPureChrom™, GC grade, 99.8%, stabilized with 50–150 ppm isoamylene) were purchased from Aladdin Biochemical Technology Co., Ltd. All reagents were used as received without further purification.

Ink Preparation: The ink was prepared via a two-step mechanical dispersion approach. Briefly, 1.0 g of Fe_3O_4 nanoparticles and 0.2 g of tBC plasticizer were suspended in 4.0 g of DCM solvent, followed by mechanical shaking with a vortex mixer (BKMAMLAB, VM-3D) for 30 min to achieve initial particle dispersion. Subsequently, 1 g of PLA/PLGA polymer blend with a mass ratio of 7:3 (0.7 g PLA and 0.3 g of PLGA) was added to the suspension. The mixture was further subjected to mechanical vibration for at least 2 h until the polymers were fully dissolved and a homogeneous magnetic viscous ink was obtained.

Preparation of Supporting Bath

Pluronic F-127 (P434421, CAS 9003-11-6) was purchased from Aladdin Biochemical Technology Co., Ltd. A 22 wt% Pluronic F-127 aqueous support bath was prepared by dissolving the polymer powder in deionized (DI) water. Keep stirring and treating at a low temperature in refrigerator until fully transparent. The solution spontaneously formed a yielding hydrogel matrix at room temperature (~ 25°C).

Hydrophobic Treatment

The nozzles were arranged in a petri dish, and 50 μL of 1H,1H,2H,2H-Perfluorodecyltrimethoxysilane (Shanghai Macklin Biochemical Co., Ltd.) was introduced into the dish. The dish was then covered, placed in a vacuum oven, and incubated at 60°C for 12 hours.

Printing Process

The synthesized ink was centrifuged by a planetary mixer (ARE-310, Thinky) to degas. Then the ink was loaded into a printing syringe equipped with a 150 μm inner-diameter needle. The embedded 3D printing process was executed inside the 22 wt% Pluronic F-127 supporting bath at room temperature. The printing parameters were precisely controlled with a pneumatic extrusion pressure of 10 psi (~ 68.9 kPa) and a nozzle moving speed of 1.0 mm/s to ensure high-fidelity line feature control.

Post-Processing and Harvesting

Utilizing the reverse thermo-reversible phase transition behavior of Pluronic F-127 (gel-to-sol transition near 0–4°C), the container containing the printed stent was incubated in a refrigerator (~ 4°C) overnight. Upon complete liquefaction of the support bath, the free-standing magnetic stents were directly extracted and thoroughly rinsed with DI water multiple times to remove any residual Pluronic F-127.

Characterization

Magnetothermal Behavior

The magnetothermal heating performance of the printed stents was evaluated using a high-frequency alternating magnetic field (AMF) generator (purchased from Hangzhou Hanggong Electrical Technology Co.Ltd) operating at an output power of 3 kW and a frequency of approximately 50 kHz. The temporal surface temperature distribution of the stents during AMF exposure was dynamically monitored and recorded using an infrared thermal camera (TiS55+, Fluke Corporation).

Shape Memory Recovery

To assess shape memory behaviors, the printed stent was first programmed into a temporary deformed state above its glass transition temperature (~ 60 ℃) and subsequently cooled down to room temperature to fix the temporary shape. Upon application of the AMF, inductive magnetothermal heating rapidly elevated the stent temperature above 40°C, triggering the shape memory effect and achieving complete autonomous shape recovery within 1 min.

Shape memory performance of the samples were recorded with a camera and can be evaluated by manual measurement of the angle change. Shape recovery ratio (R_r) was calculated as follows:

$$R_r = \frac{\theta_b - \theta_{rec}}{\theta_b - \theta_0} \times 100\%$$

where θ_0 represents the original angle, θ_b is the bended angle, and θ_{rec} is the recovered angle[36,37].

Rheological Properties

The rheological behaviors of the Pluronic F-127 supporting bath were characterized using a rotational rheometer (ARES-G2, TA Instruments) equipped with a 25 mm plane plate at 1 mm separation and 25°C. The support matrix with each content of Pluronic F-127 was separately loaded between the plates and scraped using a spatula to ensure a clean edge. The G' and G" were measured under oscillatory mode with a frequency of 1 Hz and a strain ranging from 0.01% to 1000%. The yield stress σ_y for each sample was defined as the shear stress at the crossover between G' and G"[38]. The response time of viscosity with a sudden drop of shear rate was performed under the transient testing mode, at a shear rate of 10 s^{-1} for 200 s at the beginning, and then the shear rate decreased abruptly to 0.01 s − 1 for another 200 s. For cyclic moduli recovery experiments, low (0.01%) and high (100%) strain were alternately applied for 60 s, at a frequency of 1 Hz.

Mechanical Testing

The mechanical properties and thermomechanical shape-memory characteristics of the printed stents were quantitatively measured using a dynamic mechanical analyzer (DMA 850, TA Instruments). For the compression experiments, a uniaxial compressive displacement of 2 mm with 0.2 mm/min was applied

to each sample. For the cycling compression experiment, a uniaxial compressive displacement of 2 mm with 0.2 mm/min was applied 5 times to the sample[15,39].

Declarations

Competing interests

The authors declare no competing interests.

Author contributions

Wenrui Zhang: conceptualization, methodology, data curation, writing—original draft, writing—review and editing. Shiqi Hu: methodology, data curation, writing—original draft, writing—review and editing. Yijie Bian: methodology, writing—review and editing. Mei Zhou: methodology, writing—review and editing. Kai Zhuang: writing—review and editing. Zeji Sun: writing—review and editing. Xiao Xiao: writing—review and editing. Hao Jiang: writing— review and editing. Shuaiqi Liu: writing—review and editing. Xiong Zhou: writing—review and editing. Jizhuang Wang: investigation, methodology. Li Liu: investigation, methodology. Han Yu: investigation, methodology. Mojun Chen: conceptualization, investigation, methodology, supervision, writing—review and editing.

Acknowledgements

This work was supported by the 14th Five-Year Plan Key R&D Plan of the Ministry of Science and Technology of the People’s Republic of China (grant no. 2024YFB3409002), the National Natural Science Foundation of China (grant nos. 22575102, 22275073 and 12302142), the U40 Project of the Ministry of Education of the People's Republic of China (grant no. SRICSPYF-BS2025025), the Guangdong Basic and Applied Basic Research Foundation (grant no. 2025B1515020073), the HKUST–HKUST(GZ) Collaborative Research Scheme (grant no. G035), the Yangcheng Scholars Research Project–Leading Talent Training Project (grant no. 2024312156), the Guangzhou–HKUST(GZ) Joint Funding Scheme (grant no. 2023A03J0157), the Guangzhou Basic and Applied Basic Research Project (grant no. 2024A04J4765) and the Shenzhen Basic Research Project (grant no. JCYJ20220530114417040). S.H. acknowledges the InnoCORE program (N10260002) of the Ministry of Science and ICT of the Korean government. The authors acknowledge the support from the MCPF (Materials Characterization and Preparation Facility) and MDMF (Materials, Design and Manufacturing Facility) at HKUST (GZ).

Data availability

All data supporting the findings of this study are included in the main text and Supplementary Materials.

References

1. Wang, T. *et al*. Adaptive wireless millirobotic locomotion into distal vasculature. *Nat. Commun.* 13, 4465 (2022).
2. Iacovacci, V., Diller, E., Ahmed, D. & Menciassi, A. Medical microrobots. *Annu. Rev. Biomed. Eng.* 26, 561–591 (2024).
3. Lai, Y. *et al*. An agile multimodal microrobot with architected passively morphing wheels. *Sci. Adv.* 10, eadp1176 (2024).
4. Ding, H. *et al*. Programmable multimodal optothermal manipulation of synthetic particles and biological cells. *ACS Nano* 16, 10878–10889 (2022).
5. Wang, X. *et al*. MOFBOTS: Metal–organic-framework-based biomedical microrobots. *Adv. Mater.* 31, 1901592 (2019).
6. Lang, X. *et al*. Ultrasound-guided closed-loop control of magnetic hydrogel microrobots with adaptive gait switching. *Microsyst. Nanoeng.* 12, 257 (2026).
7. Dreyfus, R. *et al*. Dexterous helical magnetic robot for improved endovascular access. *Sci. Robot.* 9, eadh0298 (2024).
8. Tian, Z., Xue, J., Xiao, X., Du, C. & Liu, Y. Optomagnetic Coordination Helical Robot with Shape Transformation and Multimodal Motion Capabilities. *Nano Lett.* 24, 2885–2893 (2024).
9. Ligtenberg, L.-J. W. *et al*. Performance estimation and ex vivo validation of untethered magnetic robots in soft tissue. *Adv. Sci.* e77011 (2026).
10. Sui, J. *et al*. A magnetically actuated robotic capsule endoscope for in-situ visualization and microneedle-mediated targeted drug delivery in gastrointestinal tract. *Microsyst. Nanoeng.* 12, 45 (2026).
11. Versteegden, L. R. *et al*. Tubular collagen scaffolds with radial elasticity for hollow organ regeneration. *Acta Biomater.* 52, 1–8 (2017).
12. Van Daele, L. *et al*. 3D-printed shape memory poly(alkylene terephthalate) scaffolds as cardiovascular stents revealing enhanced endothelialization. *Adv. Healthc. Mater.* 13, 2303498 (2024).
13. Shen, Y. *et al*. 3D printed personalized, heparinized and biodegradable coronary artery stents for rabbit abdominal aorta implantation. *Chem. Eng. J.* 450, 138202 (2022).
14. Lin, M., Firoozi, N., Tsai, C.-T., Wallace, M. B. & Kang, Y. 3D-printed flexible polymer stents for potential applications in inoperable esophageal malignancies. *Acta Biomater*. 83, 119–129 (2019).
15. Zhou, Y. *et al*. 4D printing of shape memory vascular stent based on β-CD-g-polycaprolactone. *Macromol. Rapid Commun.* 42, 2100176 (2021).
16. Ding, Y. *et al*. 3D-printed, citrate-based bioresorbable vascular scaffolds for coronary artery angioplasty. *Bioact. Mater.* 38, 195–206 (2024)..
17. Su, L. *et al*. Modular magnetic microrobot system for robust endoluminal navigation and high–radial force stent delivery in complex ductal anatomy. *Sci. Adv.* 11, eady4339 (2025).

18. Lin, C. *et al*. Mass-producible near-body temperature-triggered 4D printed shape memory biocomposites and their application in biomimetic intestinal stents. *Compos. Part B Eng.* 256, 110623 (2023).
19. Bisht, N. *et al*. MXene enhanced shape memory polymer composites: The rise of MXenes as fillers for stimuli-responsive materials. *Chem. Eng. J.* 498, 155154 (2024).
20. He, M., Hsu, Y.-I. & Uyama, H. Design of novel poly(L-lactide)-based shape memory multiblock copolymers for biodegradable esophageal stent application. *Appl. Mater. Today* 36, 102057 (2024).
21. Guo, T. *et al*. Magnetic guidance shape memory PLA/TBC/Fe3O4 microspheres for dentin tubule sealing. *Compos. Part A Appl. Sci. Manuf.* 180, 108083 (2024).
22. Lin, C. *et al*. 4D-printed biodegradable and remotely controllable shape memory occlusion devices. *Adv. Funct. Mater.* 29, 1906569 (2019).
23. Hicks, A. J. *et al*. Polycaprolactone-based shape memory foams as self-fitting vaginal stents. *Acta Biomater.* 187, 172–182 (2024).
24. Hui, Y. *et al*. Three-dimensional printing of soft hydrogel electronics. *Nat. Electron.* 5, 893–903 (2022).
25. Karyappa, R. *et al*. 3D printing of polyvinyl alcohol hydrogels enabled by aqueous two-phase system. *Mater. Horiz.* 11, 2701–2717 (2024).
26. Eom, W. *et al*. Fast 3D printing of fine, continuous, and soft fibers via embedded solvent exchange. *Nat. Commun.* 16, 842 (2025).
27. Wehner, M. *et al.* An integrated design and fabrication strategy for entirely soft, autonomous robots. *Nature* 536, 451–455 (2016).
28. Skylar-Scott, M. A. *et al*. Biomanufacturing of organ-specific tissues with high cellular density and embedded vascular channels. *Sci. Adv.* 5, eaaw2459 (2019).
29. Karyappa, R., Liu, H., Zhu, Q. & Hashimoto, M. Printability of Poly(lactic acid) Ink by Embedded 3D Printing *via* Immersion Precipitation. *ACS Appl. Mater. Interfaces* 15, 21575–21584 (2023).
30. Xin, K. *et al*. Simultaneous strengthening and toughening of PLA with full recyclability enabled by resin-microsphere-modified L-lactide oligomers. *Chem. Eng. J.* 500, 156743 (2024).
31. Peng, W. *et al*. 4D printed shape memory anastomosis ring with controllable shape transformation and degradation. *Adv. Funct. Mater.* 33, 2214505 (2023).
32. Gao, Z. *et al.* Simultaneous multi-material embedded printing for 3D heterogeneous structures. *Int. J. Extrem. Manuf.* 5, 035001 (2023).
33. Wu, Q. *et al.* Embedded extrusion printing in yield-stress-fluid baths. *Matter* 5, 3775–3806 (2022).
34. Li, Y. *et al*. Multi-material embedded 3D printing for one-step manufacturing of multifunctional components in soft robotics. *Addit. Manuf.* 85, 104178 (2024).
35. Friedrich, L. M. & Seppala, J. E. Simulated filament shapes in embedded 3D printing. *Soft Matter* 17, 8027–8046 (2021).

36. Liu, H., Wang, F., Wu, W., Dong, X. & Sang, L. 4D printing of mechanically robust PLA/TPU/Fe3O4 magneto-responsive shape memory polymers for smart structures. *Compos. Part B Eng.* 248, 110382 (2023).
37. Li, Y. *et al.* Adaptive 4D-printed vascular stents with low-temperature-activated and intelligent deployment. *Adv. Funct. Mater.* 36, e21468 (2026).
38. Liu, Z., Bhandari, B., Prakash, S., Mantihal, S. & Zhang, M. Linking rheology and printability of a multicomponent gel system of carrageenan-xanthan-starch in extrusion based additive manufacturing. *Food Hydrocoll.* 87, 413–424 (2019).
39. Zhao, W. *et al*. Bionic design and performance research of tracheal stent based on shape memory polycaprolactone. *Compos. Sci. Technol.* 229, 109671 (2022).

Figures

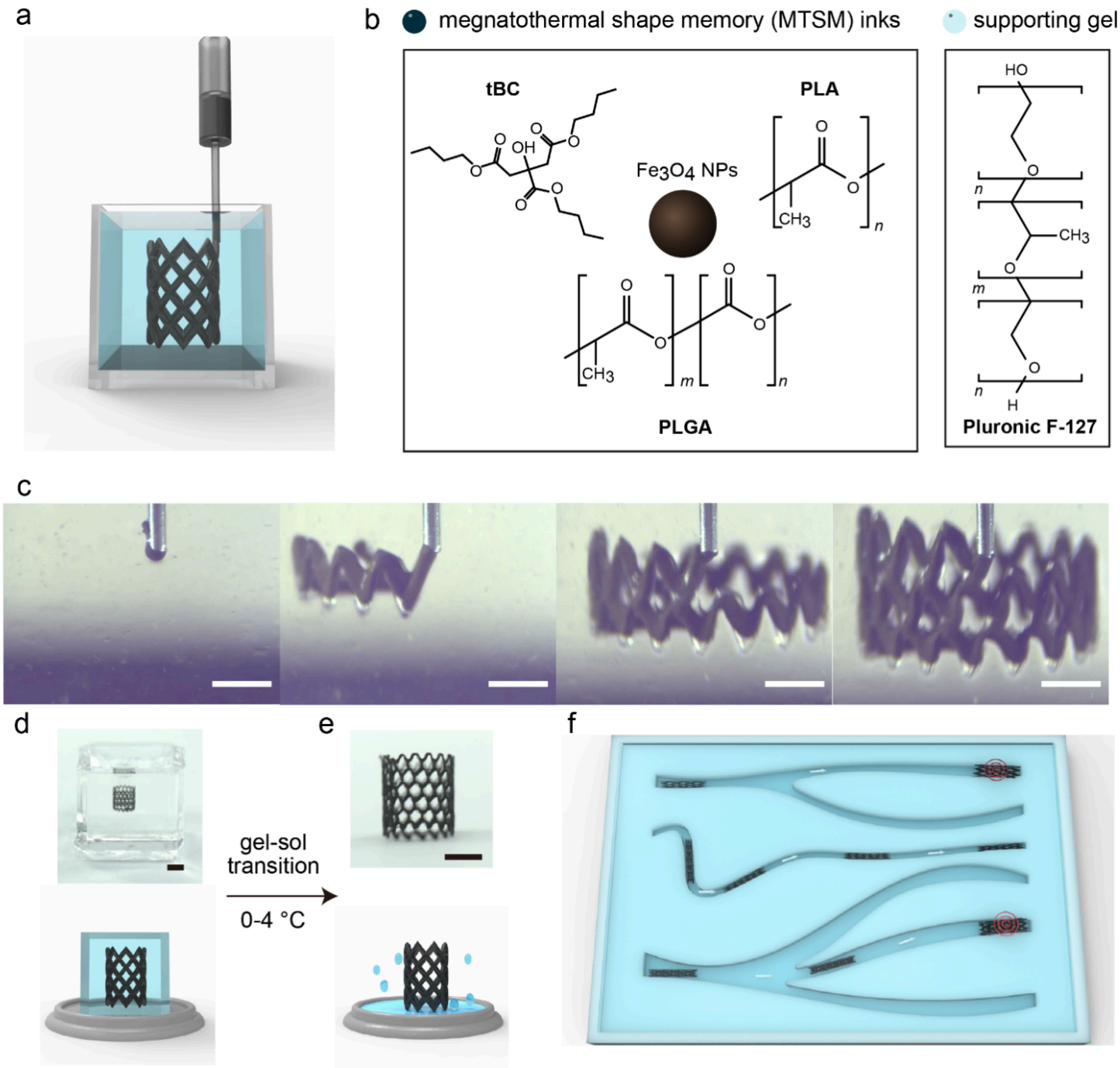


Figure 1

Embedded fabrication and operating concept of the magnetothermal shape-memory (MTSM) lattice robot. (a) A solvent-based magnetic polymer ink is extruded through a submerged nozzle into a yield-stress Pluronic F-127 support bath, which fluidizes locally around the nozzle and re-solidifies behind it, stabilizing the cylindrical lattice throughout printing. (b) Ink constituents and their assigned functions: tBC plasticizer, PLA and PLGA as the shape-memory matrix, and Fe_3O_4 nanoparticles as the dual magnetic and inductive-heating phase; Pluronic F-127 (right) is the sacrificial thermoreversible support gel. (c) Printing process of the MTSM lattice robot. Scale bar, 1 mm. (d) Printed lattice retained inside the

transparent support bath. (e) Cooling to 0–4 °C drives the gel–sol transition of Pluronic F-127 and permits non-destructive harvesting of the free-standing lattice with open pores preserved.Scale bar, 2 mm. (f) Conceptual two-stage operation in an open-top vascular-mimetic channel network: a compact, horizontally oriented robot is magnetically transported to a target (magenta arrows) and then radially expanded by AMF-triggered shape recovery (red arrows) to contact and support the channel walls.

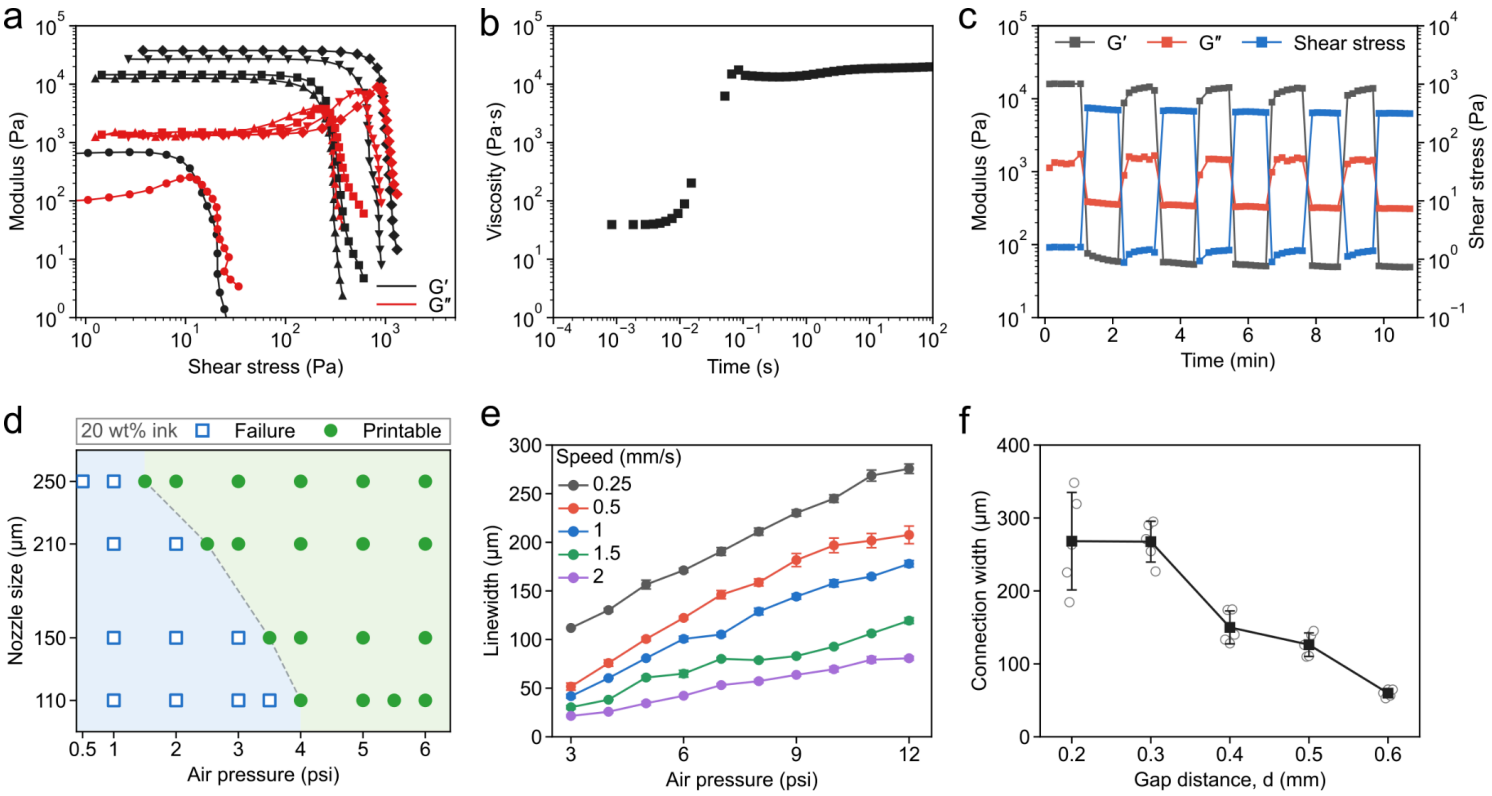


Figure 2

Rheology-guided process window and geometric control. (a) Storage modulus *G*' (black) and loss modulus *G*" (red) versus shear stress for Pluronic F-127 support baths at 18, 20, 22, 25 and 30 wt%; distinct symbols denote concentration. The *G*' = *G*" crossover defines the operational yield stress. (b) Viscosity recovery following a step decrease in shear rate from 10 to 0.01 s^{-1}, showing structural rebuild to the 10^4 Pa s range within about 0.07 s. (c) Five alternating low-strain (0.01%) and high-strain (100%) intervals; *G*' and *G*" on the left axis, applied shear stress on the right axis, demonstrating fully reversible fluidization. (d) Printability map as a function of nozzle diameter and pneumatic pressure. Open blue squares denote failed or intermittent extrusion, filled green circles denote continuous printing; the dashed line is a guide to the observed transition. (e) Filament width versus air pressure at translation speeds of 0.25, 0.5, 1.0, 1.5 and 2.0 mm s^{-1} (mean ± s.d.; *n*= 5, except 2.0 mm s^{-1} at 3 psi where *n* = 4). (f) Connection width between adjacent filaments versus programmed gap distance; open circles are individual measurements, filled squares are mean ± s.d. (*n* = 5).

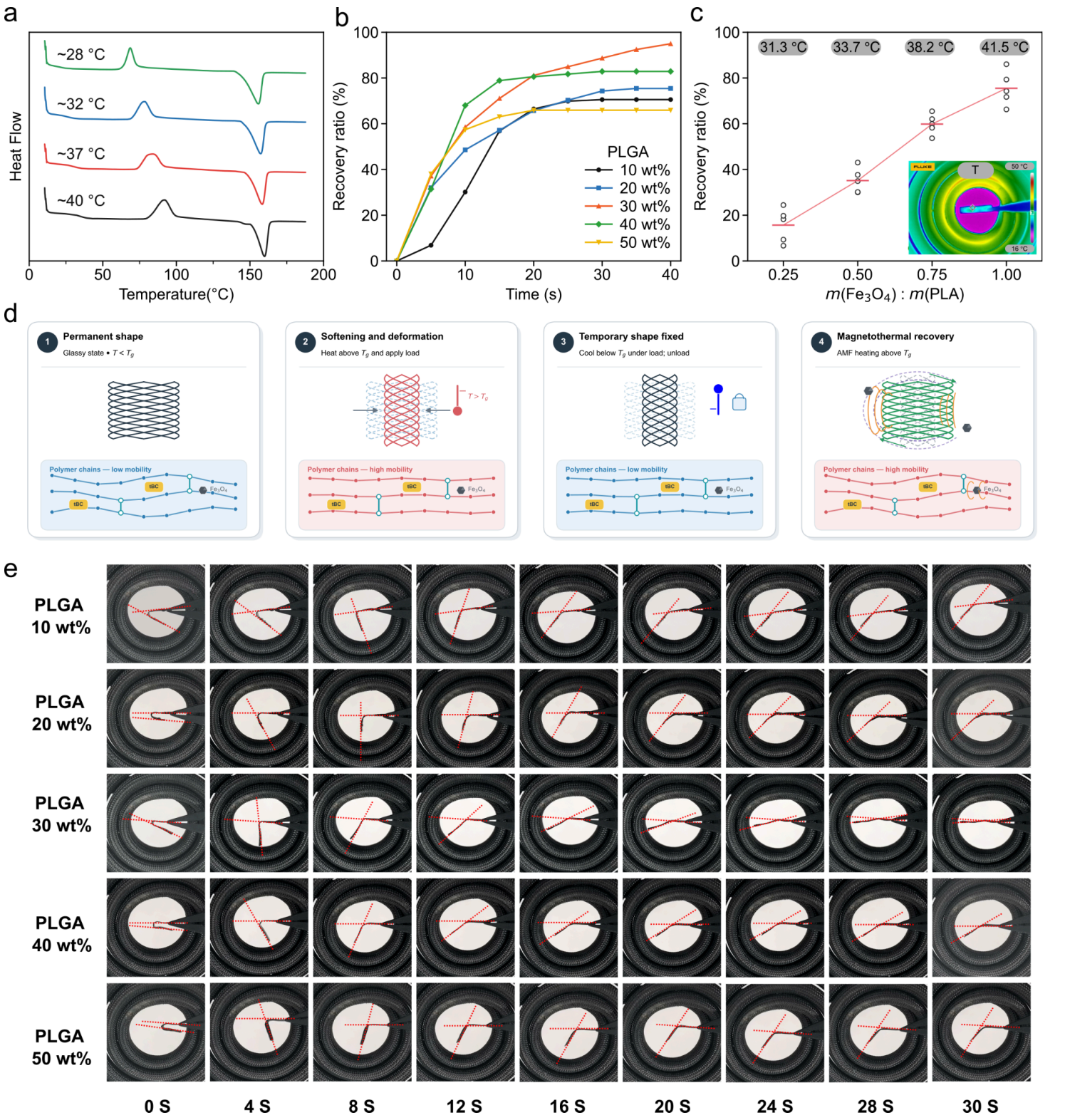


Figure 3

Compositional programming of thermal switching and magnetothermal recovery. (a) Vertically offset DSC traces showing the low-temperature switching transition shifting from about 40 to 28 °C as tBC increases from 15 to 30 wt. (b) Recovery kinetics for 10–50 wt% PLGA over 40 s of AMF exposure. The dependence is non-monotonic, with 30 wt% giving the highest final recovery (about 95%) and 40 wt% the fastest early response. (c) Recovery ratio versus nominal Fe_3O_4:PLA mass ratio, with individual

measurements (open circles), means (line), and the corresponding steady-state magnetothermal temperatures (grey labels); inset, representative infrared thermogram showing localized heating (n = 5). (d) The four-step thermomechanical cycle: permanent shape in the glassy state; softening and radial compression above T_g; fixation of the compact temporary shape on cooling under load; and AMF-triggered magnetothermal recovery. Lower panels show the corresponding chain-mobility states. (e) Time-lapse angular recovery over 0–30 s for the five PLGA fractions; dashed red lines mark the instantaneous strut angle.

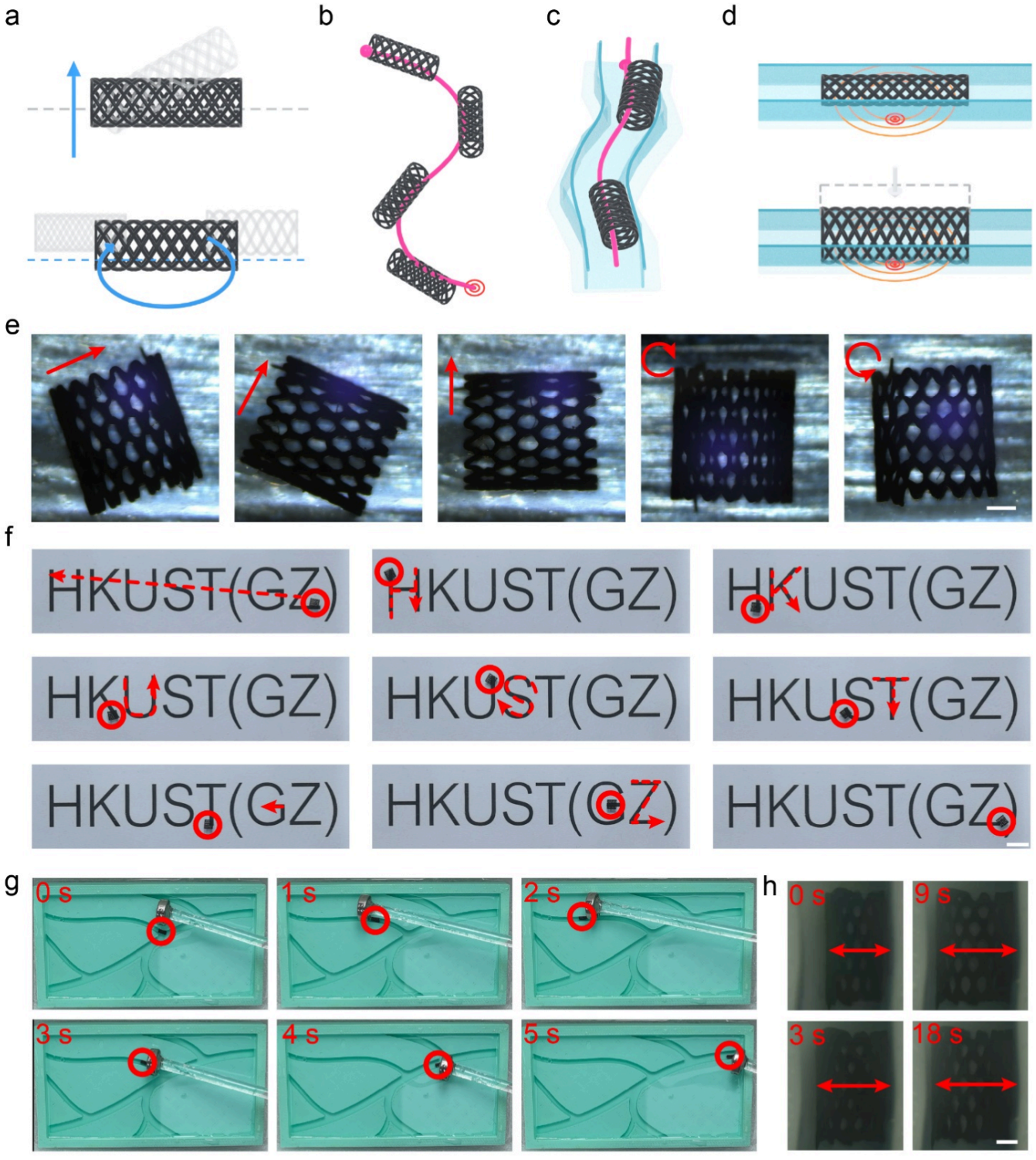


Figure 4

Magnetic pose control, programmed navigation, and target-site magnetothermal deployment. (a) Schematic of pose control: a change in quasi-static field direction reorients the compact lattice (top), while a rotating field drives continuous rotation about the long axis (bottom). (b) Schematic of gradient-driven trajectory following, with the commanded path in magenta. (c) Schematic of navigation through a confined, curved fluidic channel. (d) Schematic of site-specific deployment: the compact robot is positioned within the channel (top) and AMF exposure triggers radial expansion into wall contact (bottom); orange contours denote the AMF region. (e) Optical images of the robot under quasi-static field control. The first three panels show reorientation of the long axis to distinct commanded headings (straight red arrows); the final two show continuous rotation under a rotating field (circular red arrows). Scale bar, 1 mm. (f) Gradient-driven navigation along the complete “HKUST(GZ)” trajectory. The robot (red circle) is steered sequentially along each character; dashed red lines indicate the executed path. Scale bar, 10 cm. (g) Navigation through a FDM-printed vascular-mimetic channel network filled with fluid, imaged from above at 1 s intervals from 0 to 5 s. (h) AMF-triggered radial deployment at the target site in a straight groove of 4 mm width, imaged at 0, 3, 9 and 18 s. Red double-headed arrows indicate the instantaneous lattice width, measured between the outer edges of the lattice normal to the groove axis, which increases from 2.60 to 3.85mm while axial length is approximately preserved. Scale bar, 1mm.

Supplementary Files

This is a list of supplementary files associated with this preprint. Click to download.

- s4.mp4
- SupportingInformation.docx
- s5.mp4
- s1.mp4
- s2.mp4
- s6.mp4
- s3.mp4